Thermomagnetic convective flows in a vertical layer of ferrocolloid: Perturbation energy analysis and experimental study

Sergey A. Suslov*
Mathematics H38, Swinburne University of Technology, Hawthorn, Victoria 3122, Australia

Alexandra A. Bozhko, Alexander S. Sidorov, and Gennady F. Putin
Department of Physics, Perm State National Research University, 15 Bukirev Street, Perm 614990, Russia
(Received 30 December 2011; revised manuscript received 13 March 2012; published 5 July 2012)

Flow patterns arising in a vertical differentially heated layer of nonconducting ferromagnetic fluid placed in an external uniform transverse magnetic field are studied experimentally and discussed from the point of view of the perturbation energy balance. A quantitative criterion for detecting the parametric point where the dominant role in generating a flow instability is transferred between the thermogravitational and thermomagnetic mechanisms is suggested, based on the disturbance energy balance analysis. A comprehensive experimental study of various flow patterns is undertaken, and the existence is demonstrated of oblique thermomagnetic waves theoretically predicted by Suslov [Phys. Fluids **20**, 084101 (2008)] and superposed onto the stationary magnetoconvective pattern known previously. It is found that the wave number of the detected convection patterns depends sensitively on the temperature difference across the layer and on the applied magnetic field. In unsteady regimes its value varies periodically by a factor of almost 2, indicating the appearance of two different competing wave modes. The wave numbers and spatial orientation of the observed dominant flow patterns are found to be in good agreement with theoretical predictions.

DOI: 10.1103/PhysRevE.86.016301 PACS number(s): 47.65.Cb, 44.25.+f, 47.20.Bp, 47.54.−r

I. INTRODUCTION

Artificial nonconducting magnetocolloids (ferrofluids) have found a variety of applications thanks to their ability to respond strongly to externally applied magnetic fields created by ordinary permanent or electromagnets. This is in contrast to paramagnetic fluids such as liquid oxygen [1,2] or gadolinium-based fluids that require much stronger fields created by superconducting magnets [3,4]. Well-known uses of ferromagnetic fluids include hydrosealing of gaps between moving parts of mechanisms, targeted drug delivery, tumor treatment, and cooling of loudspeakers, to name a few [5,6]. There are also a growing number of emerging applications that have been suggested in recent years. A magnetic fluid was used to measure the void fraction [7] and bubble speed [8] in gas-liquid systems. Magnetic fluid actuators and micropumps were suggested in [9] and references therein. The magnetocaloric effect and the ability of magnetic fluids to flow in a magnetic field without being mechanically forced prompted the design of miniature automatic cooling devices for electronics [10,11].

The current study is motivated by our interest in a relatively new application of nonconducting ferrofluids as the working fluid in heat management systems operating in reduced gravity conditions on orbital stations where cooling by natural gravitational convection cannot be achieved [12–15]. Nonuniform heating results in a nonuniform magnetization of a ferrofluid placed in an external magnetic field. Subsequently, a ponderomotive force arises that drives cooler and thus more strongly magnetized fluid particles [5] to the regions with a stronger magnetic field [16]. This motion is known as magnetoconvection. It can be initiated at normal gravity as well as in gravity-free conditions. A number of relevant numerical and experimental studies have been reported in the recent literature. For example, it was found in [17,18] that magnetoconvection can significantly intensify the heat transfer rate across a fluid-filled cavity in comparison with the regime of pure gravitational convection. In contrast, the authors of [19] found that a small-amplitude sinusoidal temperature modulation at the boundaries of a horizontal ferrofluid layer can suppress magnetoconvection, offering a means of its control. Our present work focuses on the analysis of physical mechanisms that could be responsible for such variations of the heat transfer rate rather than on quantifying them.

The geometric setup we analyze here is prompted by the configuration of likely applications that is closer to a flat layer than to other commonly studied cylindrical or spherical convection geometries. In our previous work [20] we discussed a few analogies of the current problem with convection in vibrating [21,22] and dielectric fluid layers [23] that become evident in the zero-gravity limit. Further similarities could be seen with a much studied (mostly in the context of convection in rotating planetary atmosphere) vertical annulus configuration with a heated outer surface and walls corotating about the axis of the annulus. In this case a centrifugal rather than magnetic force acts on the fluid normally to the walls. The two problems become geometrically similar when a very narrow annulus of large diameter is considered. However, there are a number of other conditions (see Sec. V) that must also be met to enable a meaningful qualitative comparison with our current results. To the best of our knowledge these were not satisfied in any of the published studies to date. Yet to put the problem in a wider context we mention a few of the most relevant rotational convection publications below.

In order to make analytical progress it is often assumed that the gravity acting along the axis of an annulus can be neglected in comparison with the centrifugal force acting radially. In

*ssuslov@swin.edu.au

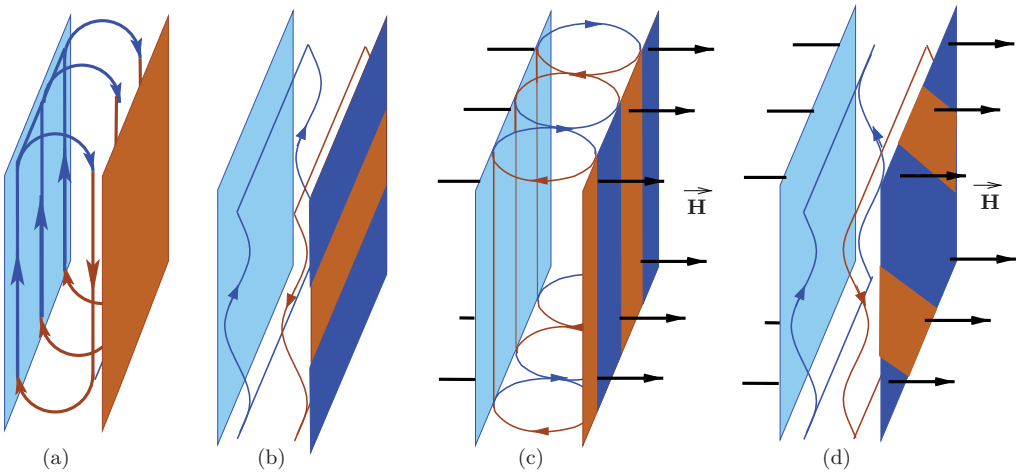

FIG. 1. (Color online) Schematic diagram of main flow patterns: (a) basic flow; (b) thermogravitational waves; (c) stationary vertical thermomagnetic rolls; (d) oblique thermomagnetic waves.

this case the rotating convection problem becomes similar to a Rayleigh-Bénard layer "wrapped around" a cylindrical surface [24]. It has been found that convection can take various forms under such an approximation. A linear stability analysis shows that stationary vertical rolls aligned with the axis of rotation are preferred. This was confirmed experimentally for relatively small supercritical Rayleigh numbers [25]. Similar vertical rolls were discovered a few years earlier in our experiments with a vertical layer of magnetic fluid [26]. More interestingly, experiments in a layer of magnetic fluid discovered the existence of inclined convection rolls [27]. Later they were also detected in a rotating annulus filled with nonmagnetic fluid [25]. In spite of these apparent similarities the reasons for the specific spatial orientation of such rolls are completely different. It is shown in [24] that the vertical rolls in rotational convection are preferred due to the action of the Coriolis force. Yet convection rolls in magnetic fluids are aligned by the fluid's up-down flow caused by the gravitational buoyancy acting along the layer [20], which is neglected in [24]. Such a flow was accounted for in [28], but, unfortunately, the large-Prandtl-number regimes characterized by oscillatory instability that is most relevant to the present study were not discussed in detail there. Therefore, we are led to the conclusion that, despite the seeming similarity between the problems of magnetoconvection in a vertical layer and of rotational convection in an annulus, currently, a direct analogy between the two cannot be established. Moreover, the oblique thermomagnetic waves predicted computationally in [20] are confirmed in our current experiments. Prior to proceeding with their analysis we briefly summarize the major findings of our previous studies below.

A series of earlier experiments [26,29,30] conducted in a thin disk-shaped vertical cavity of aspect ratio (diameter to thickness) 21.4 showed that magnetoconvection can play a dominant role in a vertical layer geometry. The resulting convection patterns were found to be drastically different from those expected to exist in a differentially heated vertical layer of nonmagnetic fluid, due to thermogravitational instability. In particular, in a large-Prandtl-number fluid, such as the kerosene-based ferrocolloid used in our experiments, the thermogravitational instability arising at sufficiently large values of the Grashof number manifests itself as a pair of counterpropagating waves seen as horizontal rolls [31–36]; see Fig. 1(b). However the most prominent patterns observed in a magnetic field even when the values of Grashof number are below the thermogravitational instability threshold (as is the case in the experiments we report here) were found to consist of vertical rolls as schematically shown in Fig. 1(c) superimposed onto the basic flow sketched in Fig. 1(a). Yet of most interest here are the oblique wavelike patterns sketched in Fig. 1(d) and termed thermomagnetic waves. They were found in a recent linear stability study [20] when a sufficiently strong magnetic field is applied. The superposition of these distinct patterns results in 16 parametric regions in the Gr_m-Gr space for a fixed value of the considered Prandtl number $\mathrm{Pr} = 130$ (see Fig. 2 below and Fig. 12 in [20]), each corresponding to its own type of a (three-dimensional) convection pattern. Although the four compounding patterns—thermogravitational waves, thermomagnetic waves of two kinds, and stationary thermoconvective rolls—were described in [20] neither the quantitative criterion defining the transition between thermogravitational and thermomagnetic waves nor the experimental evidence of the existence of these patterns has yet been obtained in extended geometries (such as the rectangular layer of large aspect ratio 41.6 used in the current experiments). Filling this gap is the major purpose of the present work. The perturbation energy balance analysis [37–39] that enables us to pinpoint physical mechanisms driving instability of the basic flow will be developed in Secs. II and III, and the experimental observations of predicted patterns including oblique thermomagnetic waves will be discussed in Sec. IV.

In our present analysis we adopt the same physical assumptions as in [20]. We briefly list them below.

(1) The fluid density is described by a linear dependence on the temperature in the buoyancy term (Boussinesq approximation).

(2) The vectors of magnetic field and fluid magnetization remain codirected.

(3) The fluid is a perfect dielectric.

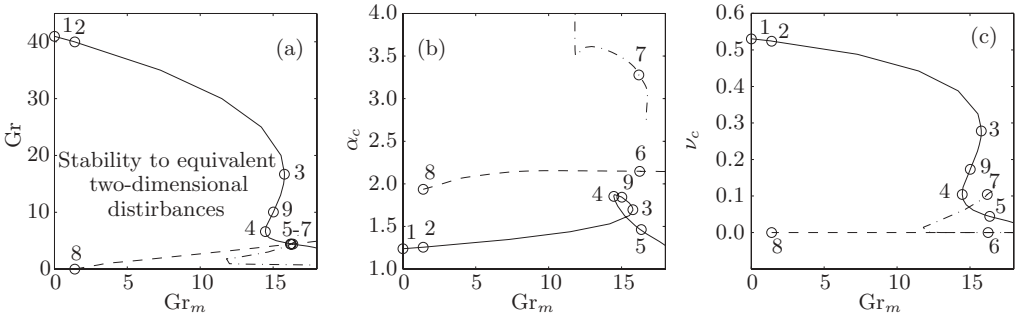

FIG. 2. Parametric stability boundary $\mathrm{Gr}(\mathrm{Gr}_m)$ (a), nondimensional critical disturbance wave number $\alpha_c(\mathrm{Gr}_m)$ (b), and nondimensional disturbance frequency $\nu_c(\mathrm{Gr}_m) \equiv \sigma_c^I/(2\pi)$ (c) for equivalent two-dimensional problem at $\mathrm{Pr} = 130$ (see [20] for details).

(4) The variation of fluid's temperature due to the magnetocaloric effect is negligible.

(5) The fluid's magnetization decreases linearly with the temperature and increases linearly with the magnetic field.

(6) The fluid is far from magnetic saturation so that its integral and differential magnetic susceptibilities are equal, i.e., the fluid operates in the linear range of Langevin's magnetization law (the value of Langevin's parameter in our experiments did not exceed 1.2).

(7) The formation of magnetic particle aggregates and their sedimentation are negligible.

(8) The variation of the fluid's viscosity due to magnetoviscous effects is negligible.

(9) The vertical thermal stratification in a fluid layer is negligible.

(10) The thermodiffusion effects are negligible.

While assumptions 1–6 are well justified experimentally, the validity of assumptions 7 and 8 in experiments is not certain. The investigation of magnetoviscous effects has become the subject of numerous dedicated studies (their discussion in the context of shear and magnetoconvection flows can be found in [5,6,40–43]). Yet no reliable constitutive model suitable for our flow conditions has been suggested to date. This forces us to adopt assumption 8. However, we are not overly concerned with neglecting possible magnetoviscous effects in our theoretical formulation as the inaccuracy introduced by this simplification is smaller than that caused by the violation of assumption 9 due to the finite aspect ratio of the used experimental chamber. We employ this last assumption in order to be able to make analytical progress. The consequence of this is that, while our past and current computational results agree qualitatively with experimental observations, it is hard to determine the accurate values of the nondimensional governing parameters involving viscosity for all experimental regimes. This problem is well known in the ferrofluid community and currently does not have a straightforward solution. A further discussion is given in Sec. IV.

Regarding assumption 10, we note that thermodiffusion (or, more precisely, thermophoresis) is always present in nonuniformly heated nanofluids such as the ferrofluid used in our experiments [44–46]. There also exists an experimental indication that in strong magnetic fields and at large temperature gradients thermophoresis can influence the distribution of solid magnetic phases in a fluid. However, noticeable variations were observed [47] only in magnetic fields at least twice as strong as, and for the cross-layer thermal gradients an order of magnitude larger than, those in our experiments. Thus assumption 10 appears to be acceptable. Despite these simplifications in the analytical formulation, the qualitative agreement between experimentally and computationally discovered features is found to be convincing, which confirms that the adopted analytical model is capable of capturing the major qualitative flow features.

Finally, prior to proceeding with presenting our current study we specifically note a recent paper [48] where the authors extended the study of [20] and investigated the parametric dependence of magnetoconvection flows in a vertical layer on the fluid's Prandtl number and on the degree of the fluid's magnetic saturation. Namely, the linear magnetization law in assumption 5 above was replaced with Langevin's nonlinear variation. It was shown that the Prandtl number range where thermomagnetic waves can be detected does depend on the value of the magnetic susceptibility of the fluid, but the types of the observed four basic patterns remain the same. Indirectly, this demonstrates the robustness of assumptions 5 and 6. It also shows that in the context of the current work employing assumptions 7 and 8 does not lead to any loss of important qualitative information regarding thermomagnetic flow patterns. Indeed, should magnetoviscous effects be accounted for [49] they would primarily lead to variation of the fluid Prandtl number. However, this was not found to affect the types of the observed magnetoconvective flow patterns so that the qualitative shape of the idealized stability diagram shown in Fig. 2 is expected to remain unchanged in realistic experimental conditions.

II. PROBLEM FORMULATION AND PERTURBATION ENERGY EQUATIONS

We consider a vertical layer of incompressible nonconducting ferromagnetic fluid contained in the gap between two long and wide parallel plates; see Fig. 1(a). The plates are maintained at uniform temperatures $T_* \pm \Theta$. The applied external uniform magnetic field is perpendicular to the layer. In the chosen Cartesian coordinate system (x, y), the x axis is perpendicular to the layer and the y axis is along the plates in the direction of the flow periodicity. This direction can form an arbitrary angle with the direction of gravity $\mathbf{g}$. The introduction of such a coordinate system is warranted by the generalized

Squire transformations discussed in [20] that enable us to transform a full three-dimensional linearized flow stability problem to an equivalent two-dimensional problem. It will be sufficient to limit our consideration here to such a transformed problem since the discussed physical results are insensitive to coordinate system rotation in the vertical plane introduced by Squire's transformation.

As shown in [20] the problem admits a steady parallel basic flow solution with a cubic vertical velocity profile v_0 and linear distributions of magnetic field H_0, fluid temperature θ_0, and magnetization M_0 across the gap. Nondimensionally, they are given as

$$\begin{aligned} \theta_0 &= -x, \quad v_0 = \frac{\mathrm{Gr}}{6}(x^3 - x), \\ H_0 &= N - x, \quad M_0 = \chi_* N + x, \end{aligned} \tag{1}$$

where χ_* is the integral magnetic susceptibility of the fluid (in this work we assume the linear magnetization law so that it is equal to the differential magnetic susceptibility χ), Gr is the Grashof number, and N is a coefficient depending on the strength of the external magnetic field (its numerical value is irrelevant to further discussion of theoretical results [50] that neglect magnetoviscous effects).

Assume that unsteady periodic perturbations of the form

$$[(\mathbf{v}(x), P(x), T(x), \phi(x)) \exp(\sigma t + i\alpha y) + \text{c.c.}], \tag{2}$$

where $\mathbf{v} = (u, v)$, P, T, and ϕ are perturbations of the fluid velocity, pressure, temperature, and magnetic potential, respectively, $\sigma = \sigma^R + i\sigma^I$ is the complex amplification rate, α is a real wave number in the y direction, and c.c. denotes the complex conjugate of the expression in brackets, are superimposed on such a flow. Then the resulting nondimensional continuity, x and y momentum, thermal energy, and magnetization perturbation equations linearized about the basic flow become [20]

$$Du + i\alpha v = 0, \tag{3}$$

$$\sigma u = (D^2 - \alpha^2 - i\alpha v_0)u - DP - \mathrm{Gr}_m D H_0 \theta - \mathrm{Gr}_m \theta_0 D^2 \phi, \tag{4}$$

$$\sigma v = -Dv_0 u + \left(D^2 - \alpha^2 - i\alpha v_0\right) v - i\alpha P + \mathrm{Gr}\theta - i\alpha \mathrm{Gr}_m \theta_0 D\phi, \tag{5}$$

$$\sigma\theta = -D\theta_0 u + \left(\frac{D^2 - \alpha^2}{\mathrm{Pr}} - i\alpha v_0\right)\theta, \tag{6}$$

$$\left(D^2 - \frac{1 + \chi_*}{1 + \chi}\alpha^2\right)\phi - D\theta = 0, \tag{7}$$

where $D \equiv \frac{d}{dx}$. The above equations along with the boundary conditions

$$u = v = \theta = 0 \ \text{ and } \ (1 + \chi)D\phi \pm \alpha\phi = 0 \quad \text{at } x = \pm 1 \tag{8}$$

define a generalized eigenvalue problem for the complex amplification rate σ which has been solved in [20]. Three nondimensional parameters appearing in Eqs. (4)–(6), the thermal and magnetic Grashof numbers $\mathrm{Gr} = \rho_*^2 \beta_* \Theta g d^3/\eta_*^2$ and $\mathrm{Gr}_m = \rho_* \mu_0 K^2 \Theta^2 d^2/[\eta_*^2(1 + \chi)]$ and the Prandtl number $\mathrm{Pr} = \eta_*/(\rho_* \kappa_*)$, where β_* and κ_* are the coefficients of thermal expansion and diffusivity (both evaluated at T_*), $\mu_0 = 4\pi \times 10^{-7}$ H/m is the magnetic constant, and $g = |\mathbf{g}|$, characterize the importance of buoyancy and magnetic forces and the ratio of viscous and thermal diffusion coefficients, respectively. The reader is referred to [20] for further details.

Here we are interested in the eigenfunctions $\mathbf{v}$, T, P, and ϕ computed at the representative points on the marginal stability surface found in [20] and reproduced in Fig. 2. As seen from this figure the stability boundary consists of three distinct curves. Their physical nature requires further clarification and we will achieve this by considering the perturbation energy balance in a way similar to that used (albeit in a different physical context), for example, in [37–39].

To derive the disturbance kinetic energy equation [51] we multiply the momentum equations (4) and (5) by the complex conjugate velocity components $\bar{u}$ and $\bar{v}$, respectively, add them together, integrate by parts across the layer using boundary conditions (8) and the continuity equation (3), and take the real part of the result to obtain

$$\sigma^R \Sigma_k = \Sigma_{uv} + \Sigma_{\mathrm{Gr}} + \Sigma_{\mathrm{vis}} + \Sigma_{m1} + \Sigma_{m2}, \tag{9}$$

where

$$\begin{aligned} \Sigma_k &= \int_{-1}^{1} (|u|^2 + |v|^2)\, dx > 0, \\ \Sigma_{uv} &= -\int_{-1}^{1} Dv_0 \mathrm{Re}(u\bar{v})\, dx, \quad \Sigma_{\mathrm{Gr}} = \int_{-1}^{1} \underbrace{\mathrm{GrRe}(\theta\bar{v})}_{E_{\mathrm{Gr}}}\, dx, \\ \Sigma_{\mathrm{vis}} &= -\alpha^2 E_k - \int_{-1}^{1} (|Du|^2 + |Dv|^2)\, dx < 0, \\ \Sigma_{m1} &= \int_{-1}^{1} \underbrace{-\mathrm{Gr}_m D H_0 \,\mathrm{Re}(\theta\bar{u})}_{E_{m1}}\, dx, \\ \Sigma_{m2} &= \int_{-1}^{1} \underbrace{\mathrm{Gr}_m D\theta_0 \,\mathrm{Re}(D\phi\,\bar{u})}_{E_{m2}}\, dx. \end{aligned} \tag{10}$$

Clearly, Eq. (9) is simply an integrated form of the linearized equations (3)–(5), but it enables one to do what cannot be achieved using the original equations solved in [20], namely, to directly and unambiguously determine the main instability mechanism. Here this will be done simply by inspecting the signs and relative magnitudes of terms entering Eq. (9) and judging their direct contribution to the disturbance amplification rate σ^R. Importantly, all information required to make physical conclusions based on this equation is local, i.e., the physical flow instability is classified directly at a given parametric point without any need to refer to a global stability diagram such as the one shown in Fig. 2. Each of the integral terms (10) has a distinct physical meaning: Σ_k is the kinetic energy of perturbations, Σ_{uv} is the energy exchange between the basic flow and the disturbance velocity fields, Σ_{Gr} is the energy contribution due to buoyancy, and Σ_{vis} is the negatively defined viscous dissipation. Because within the framework of linearized disturbances the eigenfunctions are defined up to a multiplicative constant, without loss of generality we normalize the perturbation kinetic energy balance equation (9) so that $\Sigma_{\mathrm{vis}} = -1$. The remaining two terms, Σ_{m1} and Σ_{m2}, are both due to magnetic effects. However they have

a different physical nature. Σ_{m1} accounts for the disturbance kinetic energy variation due to the thermal disturbances in the field. They influence the degree of local fluid magnetization and the appearance of a magnetic force driving cool strongly magnetized fluid particles to the regions of stronger magnetic field. On the other hand, Σ_{m2} contains perturbations of the magnetic field itself that are caused by the cross-layer motion of a nonuniformly heated fluid. This is essentially an energy perturbation due to the magnetic induction. Given that the disturbance kinetic energy Σ_k is positively defined the basic flow can only be unstable, i.e., $\sigma^R > 0$, if the sum of terms in the right-hand side of Eq. (9) is positive. In other words, positive terms in the right-hand side of (9) unambiguously identify physical effects that lead to flow destabilization, and the comparison of the magnitudes of these terms determines the relative strength of various physical influences.

III. PERTURBATION ENERGY BALANCE

While the results presented in Fig. 2 and their three-dimensional unfoldings discussed in detail in [20] provide a comprehensive stability map of the flow, there are still several questions that remain open regarding its physical nature. Even though three distinct instability modes shown by the solid, dashed, and dash-dotted lines in Fig. 2 were identified previously, the cross-layer structure of the modes has not yet been clarified. Since ferrofluids are not transparent, a direct experimental visualization of their cross-layer motion is impossible. The perturbation energy distribution that we consider here will, however, shed light on the processes taking place inside the layer. The other aspect awaiting clarification is the distinction between two magnetically driven modes shown by the dashed and dash-dotted lines in Fig. 2. The physical behavior of the flow along the segment of the instability boundary shown by the solid line in Fig. 2 also requires a clarification. It connects, in a nonmonotonic but continuous way, the limiting regimes of pure gravitational convection ($\mathrm{Gr}_m = 0$, $\mathrm{Gr} \neq 0$, point 1) and magnetically driven flow ($\mathrm{Gr}_m \neq 0$, $\mathrm{Gr} \to 0$, the solid line segment beyond point 5). Clearly, the physical nature of the instability has to change along this curve, but where exactly this happens cannot be determined based on modal analysis of infinitesimal perturbations alone. Thus we consider a number of representative points 1–8 on the marginal stability boundary and investigate the perturbation energy balance at these points to answer the aforementioned questions.

The values of various energy balance terms have been computed at points marked by circles in Fig. 2 using expressions (10) and the integral Chebyshev collocation method suggested in [52] and adapted for general convection studies in [39] and for energy integral calculation in [53,54]. From the analysis of the computational data obtained we make the following conclusions.

(a) The contribution of the basic flow velocity to the disturbance energy balance, Σ_{uv}, can be either slightly positive or negative, but it remains close to zero in all regimes; see the dashed line in Fig. 3. Therefore the interaction of the disturbance velocity field with the basic flow is weak. This confirms that instability associated with the presence of an inflection point in the basic flow velocity profile, which is the dominant instability in similar flows of low-Prandtl-number fluids (see, for example, [39,55]) does not occur in the current case of a fluid with $\mathrm{Pr} = 130$.

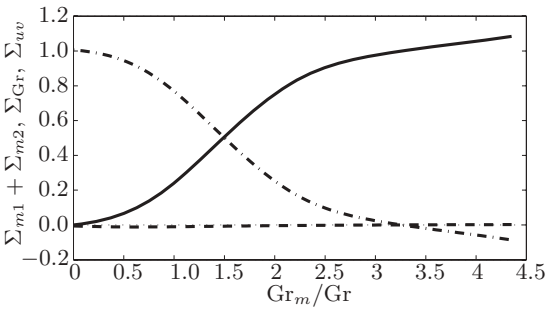

FIG. 3. The perturbation energy integrals characterizing thermomagnetic ($\Sigma_{m1} + \Sigma_{m2}$, solid line) and thermogravitational (Σ_{Gr}, dash-dotted line) mechanisms of convection and exchange with the basic flow (Σ_{uv}, dashed line) as functions of the ratio $\mathrm{Gr}_m/\mathrm{Gr}$ along the stability boundary shown by the solid line in Fig. 2(a).

(b) The thermogravitational contribution Σ_{Gr} depends strongly on the values of both Gr and Gr_m and can be either positive or negative. It is strongly destabilizing in the absence of a magnetic field, i.e., for $\mathrm{Gr}_m \sim 0$, but becomes stabilizing for larger values of Gr_m when the motion caused by the actions of the vertical buoyancy force and the horizontal magnetic ponderomotive force start competing with each other. The peculiar Z shape of the stability boundary shown by the solid line in Fig. 2(a) is the consequence of this competition: for larger values of Gr both magnetic and thermogravitational mechanisms play a destabilizing role and their combination leads to a reduction in the parametric area of the stability region (the solid line bends to the left). However, for small values of Gr the buoyancy starts playing a stabilizing role; see the dash-dotted line in Fig. 3. Figure 4 offers a possible explanation of this fact. Note that the horizontal ponderomotive magnetic force effectively drives the convection motion only during the first and third quarters of a wave period when it is aligned with the perturbation velocity; see the snapshots for $t = 0$ and $t = T/2$. At these instances cool (warm) and stronger (weaker) magnetized fluid is pushed toward the hot (cool) wall where the basic magnetic field given by (1) is stronger (weaker). It is mostly the buoyancy force that drives convection over the second and fourth quarters of the period; see the snapshots for $t = T/4$ and $t = 3T/4$. At these moments the warm (cool) fluid disturbance velocity has components up (down) and toward the warm (cool) wall. Thus work is done by the gravity force to enhance convective motion. However, work is also done by the fluid against the horizontal ponderomotive magnetic force, and this reduces the fluid's kinetic energy. At relatively large values of Gr the gravity work exceeds that done by the fluid against the ponderomotive force so that the overall buoyancy effect is destabilizing. For small values of Gr the situation is reversed and the buoyancy contribution to the disturbance energy balance becomes negative.

(c) The first of the two magnetic contributions to the energy balance, Σ_{m1}, is always non-negative. This term represents a ponderomotive force that drives more strongly magnetized cooler fluid particles into the regions of a stronger basic magnetic field, i.e., from the cool wall toward the warm one; see expressions (1). Therefore in the considered configuration

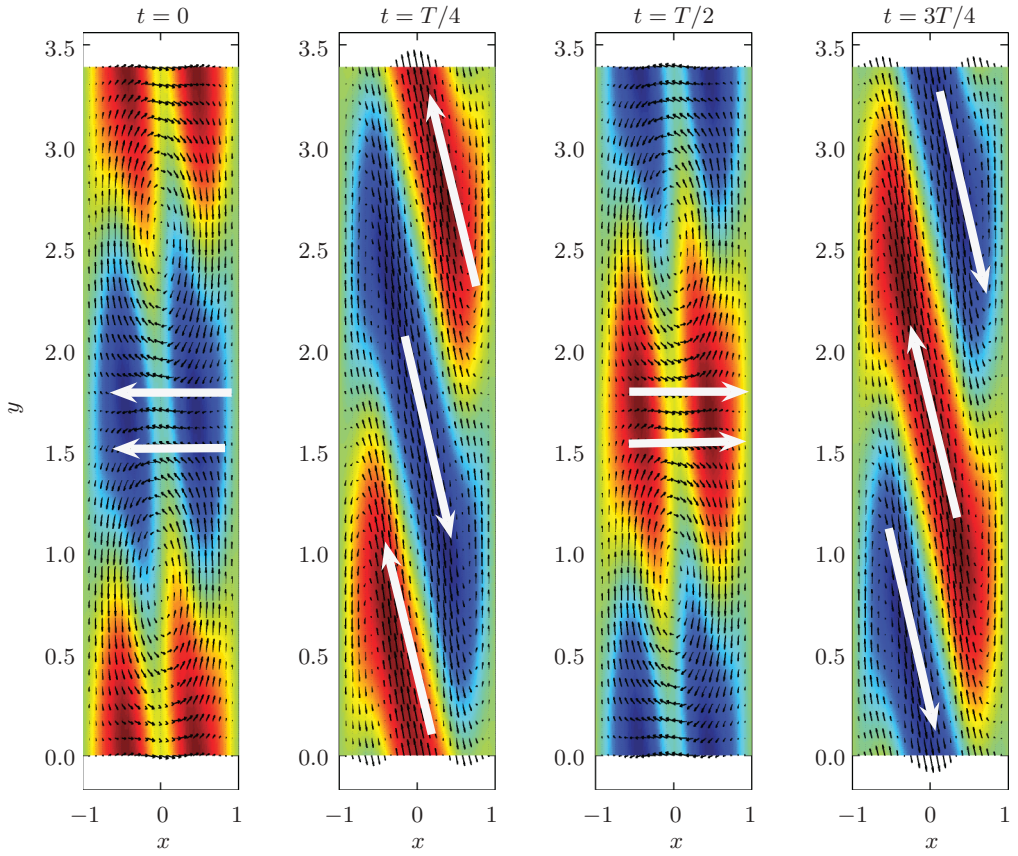

FIG. 4. (Color online) Snapshots of thermomagnetic waves (point 4 in Fig. 2) over the wave period T. Color represents the thermal field (red, warm, less dense, and more weakly magnetized fluid; blue, cool, denser, and more strongly magnetized fluid). White arrows show the dominant direction of the disturbance flow driven by the ponderomotive magnetic force.

the dependence of the fluid magnetization on the temperature always plays a destabilizing role, ultimately leading to the onset of a thermomagnetic convection.

(d) In contrast, the second magnetic term Σ_{m2} remains negative. It represents the induction of a disturbance magnetic field by the displaced ferromagnetic fluid particles. The corresponding modification of the basic magnetic field (an analogy with an electromagnetic transmitter that requires energy supply for its operation might be helpful here) always absorbs energy and thus plays a stabilizing role, hindering the change in the primary magnetization field. However, this magnetic stabilization effect is always weaker than the thermomagnetic destabilization characterized by Σ_{m1}. Therefore the overall magnetic influence in the considered geometry is always destabilizing.

The above observations enable us to draw the general conclusion that the destabilization of the primary parallel flow along the solid line in Fig. 2(a) is due to two competing physical mechanisms: the actions of ponderomotive magnetic and buoyancy forces. They also define the nature of the instability whose boundaries are shown by the dashed (points 6 and 8) and dash-dotted (point 7) lines in Fig. 2(a): purely magnetic ponderomotive force. Yet the details of these instability modes are not made clear so far. Therefore next we consider the spatial distribution of the three destabilizing integrands E_{m1}, E_{m2}, and E_{Gr}, defined in (10) and plotted in Fig. 5 for points 1–8 marked by circles in Fig. 2.

For small values of Gr_m and large values of Gr (points 1 and 2), the thermogravitational instability mechanism dominates; see the dash-dotted line in plots 1 and 2 in Fig. 5. The energy integrand E_{Gr} has two well-defined symmetric maxima near the walls. This is a reflection of the well-known fact that in large-Prandtl-number fluids such as a typical kerosene-based ferrocolloid the thermogravitational instability takes the form of two waves counterpropagating in the wall regions [33–35]. Computations show that they are almost insensitive to a magnetic field and exist even when the magnetic Grashof number is significantly increased; see the plots for points 3 and 4 in Fig. 5. However, as the ratio $\mathrm{Gr}_m/\mathrm{Gr}$ increases, the thermomagnetic effects quantitatively characterized by $E_{m1} + E_{m2}$ intensify significantly while the role of gravitational buoyancy, quantified by Σ_{Gr}, weakens. This is demonstrated in Fig. 3. The dominating role of the gravitational instability mechanism is transferred to the thermomagnetic mechanism at point 9 in Fig. 2 (which also corresponds to the intersection of the solid and dash-dotted lines in Fig. 3), where the condition

$$\Sigma_{\mathrm{Gr}} = \Sigma_{m1} + \Sigma_{m2} \tag{11}$$

is satisfied. This transition in dominance from one physical mechanism of convection to another still results in a pair of waves propagating up (down) along the hot (cold) wall. We call such waves thermomagnetic. Despite a clear difference in driving physical mechanisms the transition between them occurs in a continuous way; see the solid line in Fig. 2.

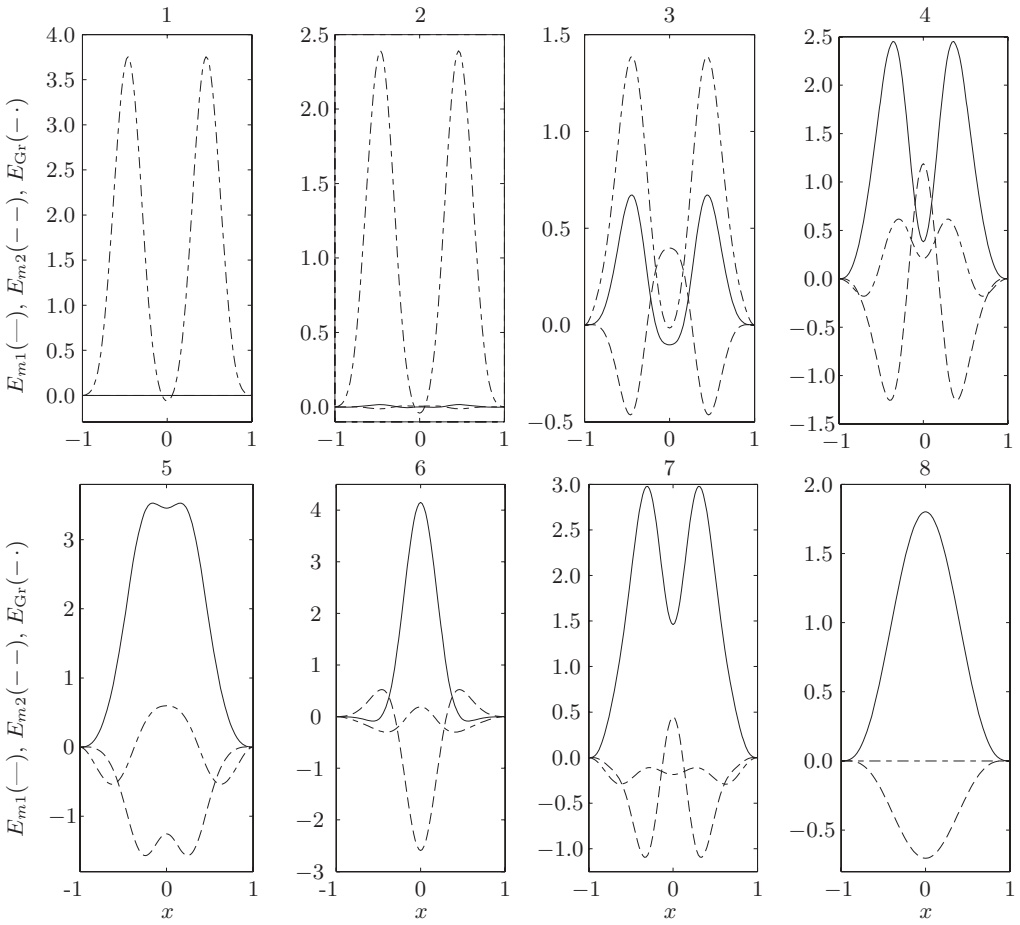

FIG. 5. Selected disturbance energy integrands for points denoted by circles in Fig. 2.

The comparison of Figs. 6 and 4 shows that the dominant component of the thermogravitational perturbation velocity field is vertical (along the layer, parallel to the gravity vector) and that of thermomagnetic waves is horizontal (across the layer, parallel to the applied magnetic field). Another distinguishing feature is the behavior of the disturbance wave numbers: when Gr_m increases so do the wave numbers of thermogravitational waves; however, this trend is reversed once they are replaced with thermomagnetic waves [see the solid line in Fig. 2(b)].

When Gr decreases the wave speeds [not shown here, but see Fig. 2(c) in [20]] also decrease, the instability pattern becomes nearly stationary, and its maximum shifts from wall regions toward the center of the layer; see the plot for point 5 in Fig. 5. The thermogravitational convection mechanism continues to play a destabilizing role in the center of the layer, but its influence in the wall regions becomes stabilizing. A shift of the instability production region to the centre of the layer has a profound effect on the characteristic wave number of the perturbations: it quickly decreases [see the right end of the solid line in Fig. 2(b)]. This has a straightforward explanation: the disturbance structures in the center of the layer near the inflection point of the basic flow velocity profile are subject to large shear forces. These forces "stretch" convection rolls, decreasing their wave number. The centrally located instability structures elongated by the shear forces then become so large that they cause a strong "flow blocking" effect. Eventually they are destroyed by the basic flow, giving way to much shorter structures; see the dash-dotted lines containing point 7 in Fig. 2. Plot 7 in Fig. 5 shows that the physical mechanism generating these flow structures is indeed the same as that for the thermomagnetic waves discussed above. Their characteristic length scale is sufficiently small (the wave number is large) so that the basic flow blocking effect is reduced and the two disturbance waves propagating along the opposite walls reappear. We also note that, although the overall magnetoinduction effect Σ_{m2} is always stabilizing, the energy integrand E_{m2} for points 3, 4, and 7 is positive in the center of the layer (between the counterpropagating thermomagnetic waves). Thus it contributes to the local destabilization near the midplane of the layer. As discussed in [20] the thermomagnetic waves are most likely to be seen in experiments as obliquely propagating patterns. This is confirmed by our observations reported in Sec. IV.

Points 6 and 8 in Fig. 2 belong to the third type of stability boundary, which is disjoint from the two segments discussed so far. The physical mechanism causing this instability is of purely thermomagnetic type: E_{m1} is strongly positive while E_{Gr} is close to zero. Therefore the gravitational buoyancy plays no essential role in these regimes of convection. The major

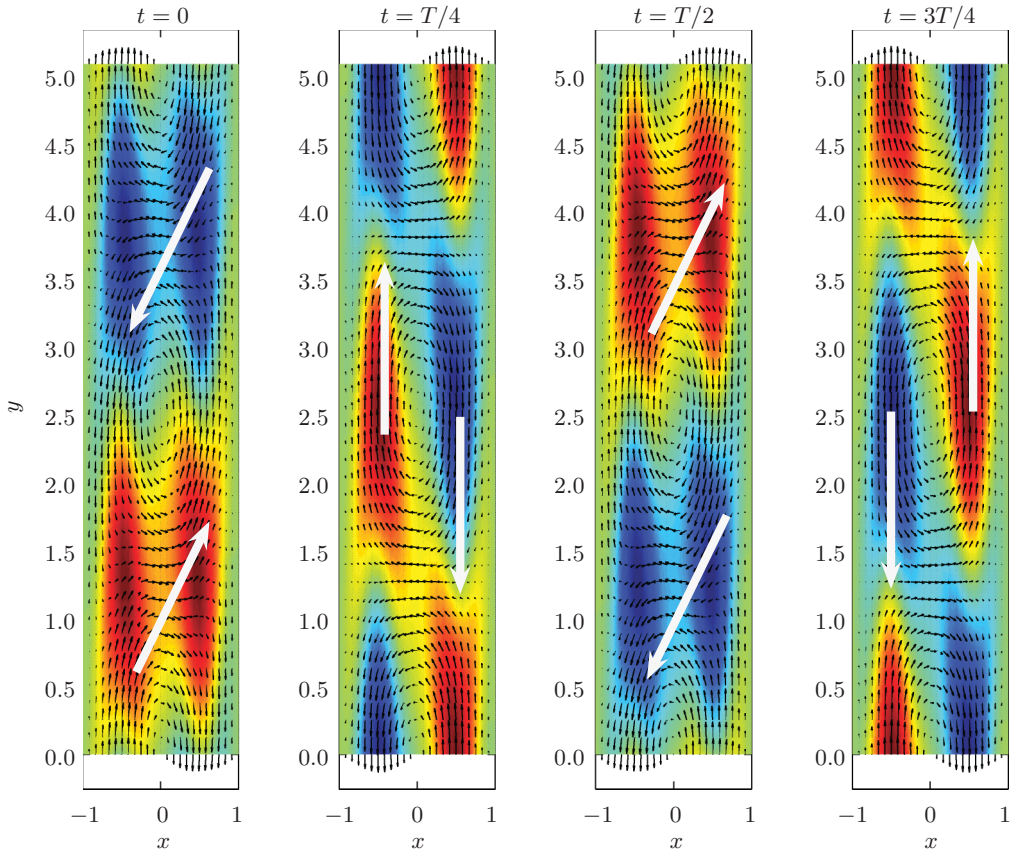

FIG. 6. (Color online) Snapshots of thermogravitational waves (point 1 in Fig. 2) over the wave period T. Color represents a thermal field (red, warm and less dense fluid; blue, cool and denser fluid). White arrows show the dominant directions of the disturbance flow driven by the buoyancy force.

destabilization occurs near the middle of the layer where basic flow velocity is zero. As a consequence, the corresponding instability patterns are stationary [20]. They take the form of vertical rolls.

IV. EXPERIMENTAL SETUP AND OBSERVED FLOW PATTERNS

In Sec. III the linearized perturbation energy balance was considered in detail, which enabled us to determine the dominant physical mechanisms driving flows in a vertical layer of ferromagnetic fluid. Here we will discuss experimental observations of flow patterns, confirming conclusions made in the previous section, and specifically the fact of the existence of thermomagnetic waves.

The schematic of the experimental chamber is shown in Fig. 7. The rectangular experimental chamber filled with a magnetic fluid (1) had the thickness $2d = 6.00 \pm 0.05$ mm, height $L = 250.0$ mm, and width $W = 70.0$ mm. The chamber was bounded on one side by a brass wall (2) of a heat exchanger with welded pipes for circulating a thermostatic fluid. A transparent heat exchanger (3) made of two Plexiglass sheets (2 and 4 mm thick), with an 8 mm gap for thermostatic fluid between them, served as the second wall. The Plexiglas frame (4) determined the inner dimensions of the working chamber. Water from two jet cryothermostats KRIO-VT-01 was pumped through the heat exchangers. The water temperature was maintained fixed within ± 0.05 K.

Since a ferrofluid is not transparent, direct observations of flow structures were impossible. Therefore a 0.1-mm-thick laminated thermosensitive liquid crystal film (5) was glued onto the inner side of a 2-mm-thick transparent Plexiglas wall of the heat exchanger (3) to enable registering the fluid temperature distribution at the cool wall of the enclosure. The sensor film was covered by a 0.075 mm laminating layer in order to protect it against erosion caused by the kerosene-based ferrofluid. The working temperature range of the thermosensitive film was 18–22 °C, corresponding to the color range from brown to green to blue. In order to achieve a near-optimal resolution of the sensor the water temperatures in heat exchangers were chosen in such a way that the average temperature of the thermosensitive film was maintained at around 20 °C. The thermal signature of the flow was photographed using an Olympus E330 camera directly connected to a computer and filmed using a Sony DCR-TRV370E digital video camera. An 18-cm-long fluorolamp was used to provide uniform lighting throughout experiments. A fluorescent lamp rather than an incandescent bulb was used to avoid parasitic heating of the experimental chamber.

A uniform magnetic field H was created by Helmholtz coils with the average diameter of 800 mm, width of 45 mm, and radial thickness of 100 mm. The distance between the

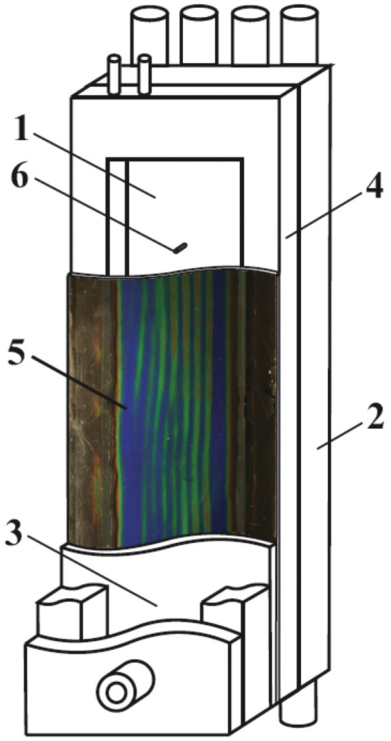

FIG. 7. (Color online) Schematic of the experimental chamber: 1, magnetic fluid layer; 2 and 3, brass and Plexiglas heat exchangers; 4, frame; 5, laminated thermosensitive liquid crystal film; 6, thermocouple.

coil centers was equal to their average radius. The magnetic field created by the coils had intensity up to 25 kA/m. A photograph and a schematic of the complete setup are shown in Fig. 8.

Experiments were performed with a kerosene-based magnetic fluid with magnetic saturation $M_S = 70$ kA/m, mean particle size of 10 nm, magnetic phase concentration of 14%, density $\rho_* = 1.44 \times 10^3$ kg/m^3, thermal expansion coefficient $\beta_* = 9.6 \times 10^{-4}$ K^{-1}, thermal diffusivity $\kappa_* = 4.3 \times 10^{-8}$ m^2/s, and initial dynamic viscosity $\eta_* = 7.66 \times 10^{-3}$ kg/(m s) (measured in the absence of a magnetic field).

At the values of Grashof number estimated in the absence of a magnetic field, the thermogravitational waves sketched in Fig. 1(b) would be expected to propagate vertically along an infinite fluid layer; see the flow stability diagram in Fig. 2(a). However, they were not detected experimentally because of the finite size of the experimental chamber that led to a vertical thermal stratification. Such a stratification suppresses both stationary [56] and wave [57] disturbances that are not caused by magnetic effects (see further discussion below). Note also that the viscosity of a ferrofluid generally depends on the applied magnetic field. One of the reasons for its change is the formation of solid particle aggregates in a fluid [41,58,59]. For example, it was shown in [42] that the viscosity of a ferrofluid placed in a magnetic field can significantly increase provided that the flow shear rate is sufficiently small. For this reason the values of the governing nondimensional parameters change during the experiment. In particular, the value of Gr $\sim 1/\eta^2$ decreases when an external magnetic field is applied, leading to the further suppression of thermogravitational waves. These factors enabled us to focus our experimental study fully on the thermomagnetic effects whose thermal signature (not obscured by thermogravitational waves) is reliably detected by a sensor film. Even though the physical processes leading to the variation of fluid properties are known and a number of constitutive relations have been suggested for simple steady flows [60,61], at present there is no reliable constitutive model for magnetoviscosity nor a definitive way of measuring it over the complete range of our specific flow conditions. Because of this currently it is impossible to accurately estimate the nondimensional parameters Gr, Gr$_m$, and Pr for all experimental conditions. Thus below we choose to report the directly measured values of the applied magnetic field H and the cross-layer temperature difference $\Delta T \equiv 2\Theta$ without converting them to the nondimensional parameters introduced in Sec. II.

The experimental runs were conducted following two scenarios: (a) increasing the cross-layer temperature difference while keeping the external magnetic field and the average

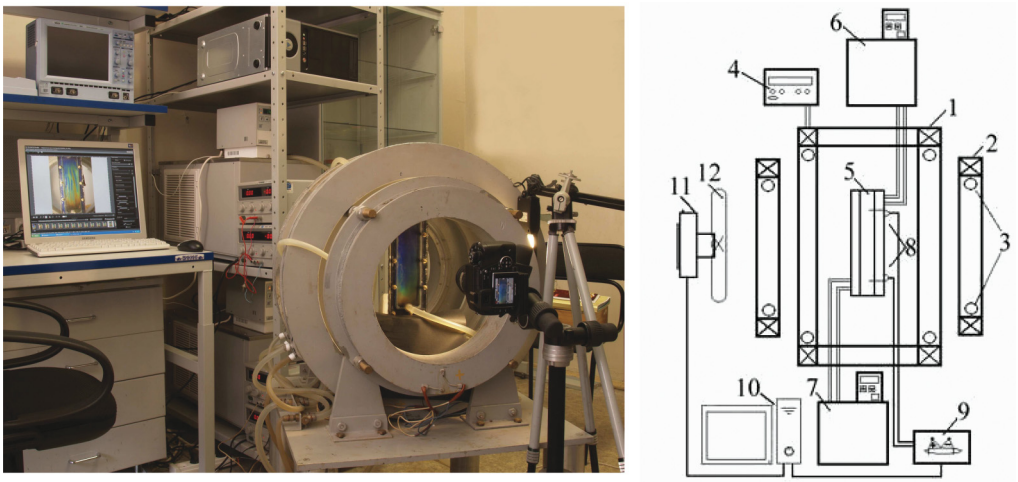

FIG. 8. (Color online) Experimental setup: 1, Helmholtz coils; 2, correcting coils; 3, cooling system; 4, dc power supply; 5, experimental chamber; 6 and 7, thermostats; 8, copper-Constantan thermocouples; 9, thermocouple signal recorder Thermodat-38V1; 10, computer; 11, photo camera; 12, fluorolamp.

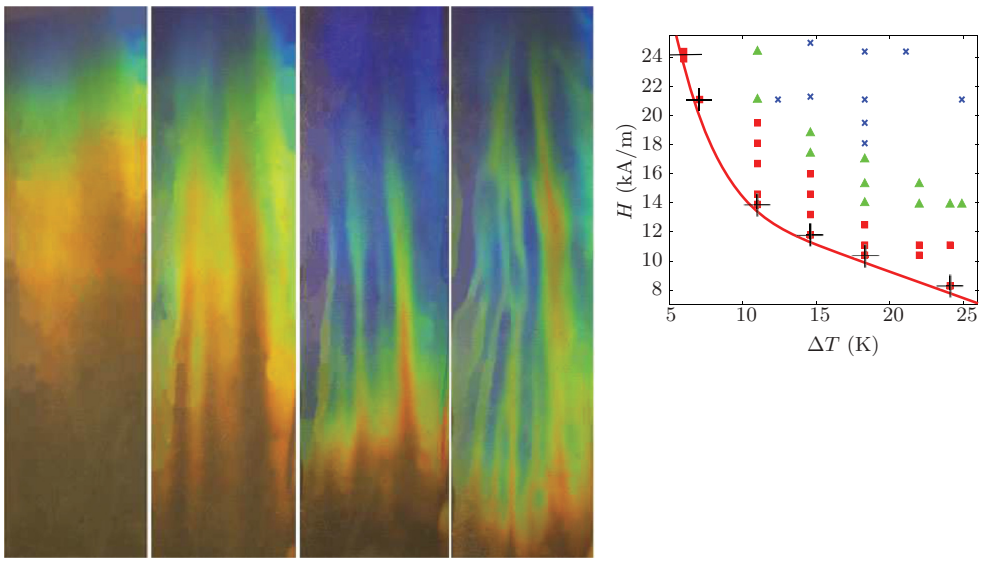

FIG. 9. (Color online) Left: snapshots of typical flow patterns observed at $\Delta T = 18.3$ K. The width of the depicted region is 58 mm. Right: experimental stability map (squares, stationary vertical thermomagnetic rolls; triangles, superposition of stationary vertical thermomagnetic rolls and oblique thermomagnetic waves; crosses, superposition of stationary thermomagnetic vertical rolls and two oblique thermomagnetic waves; solid line, basic flow stability boundary. Error bars are shown by thin horizontal and vertical lines.

fluid temperature T_* fixed and (b) strengthening the field while keeping the temperature difference fixed. Both experimental scenarios correspond to a predominantly left-right cut through Fig. 2(a) and lead to strengthening of thermomagnetic effects and the appearance of various magnetoconvective patterns; see the experimental stability map and examples of typical flow patterns in Fig. 9. Consistent with the theoretical results of [20], they fall into four general categories described in detail below.

In the absence of a magnetic field, only the primary flow exists in the chamber when the fluid rises along the warm brass wall and descends along the cooler transparent wall to which the thermosensitive film is attached. In the case of an infinite vertical fluid layer this would correspond to solutions given by expressions (1). However, since the experimental chamber had a finite vertical size, the thermal stratification seen in the leftmost image in Fig. 9 as a vertical color gradation from brown (cool) at the bottom to blue (warm) at the top was unavoidable. This in turn resulted in a spatial variation of magnetoconvective flow strength along the layer, clearly seen in the other three images in Fig. 9: the most profound patterns were observed in the cooler lower part of the chamber, where the fluid was characterized by a larger local magnetic Grashof number.

As the magnetic field was gradually increased, the first spatial pattern was observed: a set of stationary vertical rolls appearing as color stripes on the liquid crystal sensor (squares in the experimental stability map in Fig. 9). It can be shown that for a relatively slow fluid motion the heat transfer intensity across the layer and thus the local temperature of the wall registered by a sensor are proportional to the cross-layer velocity component u. Thus the blue-green stripes correspond to the locations where fluid flowing from a warm back wall impinges on the sensor and the brown stripes correspond to cool zones where the induced flow was reversed; see Fig. 1(b). The width l of the blue-brown stripe pairs was used to compute the observed nondimensional wave number α_{expt} of the pattern as $\alpha_{\text{expt}} = 2\pi d/l$. It was found to be 1.9 ± 0.1. As was discussed in [20], the appearance of stationary vertical magnetoconvection rolls does not depend on the value of the gravitational Grashof number and corresponds to point 8 in Fig. 2. The computed value of the critical wave number for magnetoconvection rolls is $\alpha = 1.936$, which agrees closely with experimental observations. Moreover, the vertical roll threshold is characterized by a fixed value of the magnetic Rayleigh number $\text{Ra}_m \equiv \text{Gr}_m\text{Pr}$ rather than the magnetic Grashof number. Since the Rayleigh number does not depend on the fluid viscosity, we can meaningfully compare its theoretical and experimental critical values, 181.74 and $(1.8 \pm 0.2) \times 10^2$ (averaged over several experimental runs with slightly different mean fluid temperatures), respectively. They are also in reasonable agreement. As was discussed in [20], stationary thermomagnetic rolls remain vertical and dominate the disturbed flow.

The further increase of the magnetic field led to the appearance of slightly oblique thermomagnetic traveling waves (triangles in the experimental stability map in Fig. 9); see the third snapshot in Fig. 9. The dynamics of such waves is illustrated in Fig. 10: they move in a direction perpendicular to the color stripes as shown by the arrows. A ruler is shown for reference along the bottom edge of each frame. The experimentally observed propagation speed was 1–2 mm/s, which falls into the range of wave speeds $c = 2\pi\nu_c/\alpha$, corresponding to the dash-dotted lines in Fig. 2 predicted theoretically. While stationary vertical rolls are still clearly seen, the inclined rolls regularly appear near the left vertical edge of the experimental chamber and move right and slightly down over the complete lateral span of the cavity.

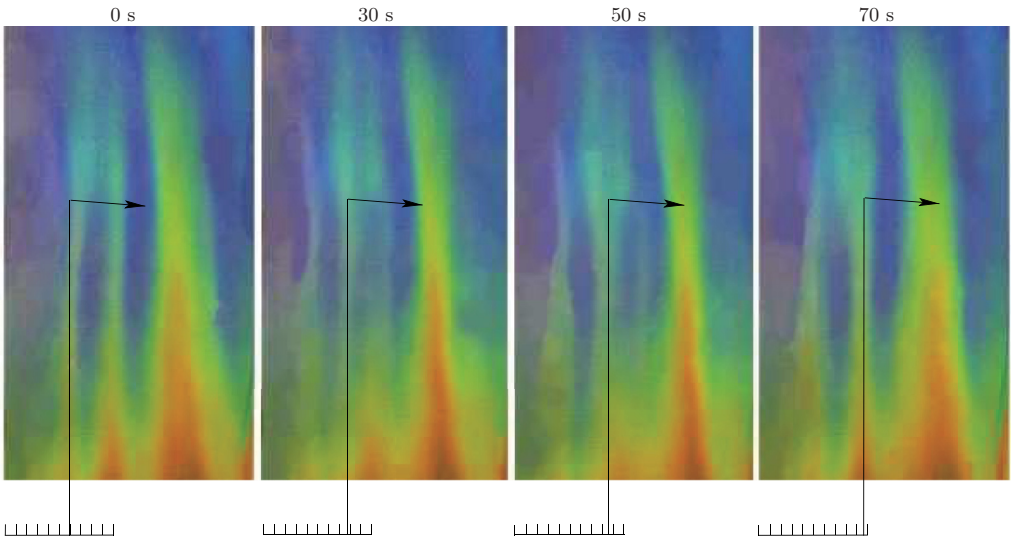

FIG. 10. (Color online) Unsteady convection rolls observed in the middle section of the experimental chamber. Arrows show the direction of roll propagation and the vertical lines trace the instantaneous location of a selected convection roll [62]. The width of the depicted region is 58 mm (divisions on the ruler are approximately 2.6 mm apart).

A video of the corresponding experimental observations is available online [62].

In even stronger magnetic fields the convection pattern becomes essentially unsteady. The rolls are noticeably sloped and propagate in the direction of their inclination (their velocity has a downward component near the cool wall). The patterns become less regular [see the image corresponding to $H = 21$ kA/m in Fig. 9 (crosses in the experimental stability map in Fig. 9)], indicating the appearance of additional waves with a different wave number that interfere with the stationary vertical rolls and oblique waves detected in weaker fields. In this regime the pattern is still dominated by stationary vertical rolls labeled as 1 and 3 in Fig. 11. However, additional rolls labeled as 2 and 4 slowly drifting from left to right (in the direction of inclination) periodically appear and disappear in between the original vertical rolls. Qualitatively this regime corresponds to the simultaneous presence of stationary magnetoconvection rolls and slowly propagating relatively weak thermomagnetic waves corresponding to the dashed and dash-dotted lines in Fig. 2(a) and characterized by a wavelength which is 1.5–1.8 times smaller than that of the stationary rolls; see Fig. 2(b). This behavior is also consistent with the theoretical findings of [20]: the observed wave number of the centrally located rolls is found to be close to the theoretical values along the solid line in Fig. 2(b). These facts indicate that the observed propagating patterns are caused by thermomagnetic waves identified near points 3–5 and 9 in Fig. 2(a) via the disturbance energy balance analysis of the previous section.

Since in our experiments the thermosensitive liquid crystal film was glued to the cool wall, only the related temperature distribution in a thin layer near the cool wall was visualized. Thus only one of the counterpropagating waves is seen in the presented experimental images. It was shown in [20] that the waves near the cool wall follow the direction of the basic flow that descends near this wall. Indeed, the rolls seen in the middle of the lower part of the experimental cavity that lean slightly to the right (see the rightmost photo in Fig. 9) move from left to right. This is consistent with the theoretical prediction for thermomagnetic waves arising near points 3–5 in Fig. 2. However, the thermal field visualization also shows that the leftmost and rightmost colored stripes move with a velocity having an upward component. This contradicts theoretical predictions. We believe that the vertical walls near the left and right edges of the experimental chamber, whose presence is not accounted for by the present analysis, could induce this motion. In order to minimize friction losses the near-edge convection rolls tend to orient themselves perpendicularly to the sidewalls as soon as they approach them. Because of the vertical stratification more convection rolls appear in the lower part of the chamber so that they approach the sidewalls there first (see the Λ-shaped color stripe formation in the rightmost image in Fig. 9). As soon as this happens the stripes representing convection rolls bend to become perpendicular to the vertical sidewalls. This deformation of convection rolls appears as an upward motion. Once the deformed roll bends upward, it reaches a hotter (due to stratification) region, where the fluid magnetization is weaker, and disappears. Its place is taken by the next roll and the process repeats.

In addition to a purely mechanical reason for the upward motion of the observed patterns along the vertical edges, the distortion of the magnetic field near the layer boundaries could also contribute to the deviation of the observed patterns from those expected theoretically in an infinite layer. This will be discussed in more detail below.

In order to obtain a quantitative record of the temperature variation in the fluid layer, a thermocouple with the diameter of wires 0.1 mm was installed in the lower part of the chamber at the location shown in the leftmost image in Fig. 9 approximately 0.75 mm away from the warm back wall of the experimental chamber and 46 mm above the bottom edge of the chamber. A second thermocouple was installed 43 mm away from the top edge of the chamber above the first one to register the vertical temperature stratification in

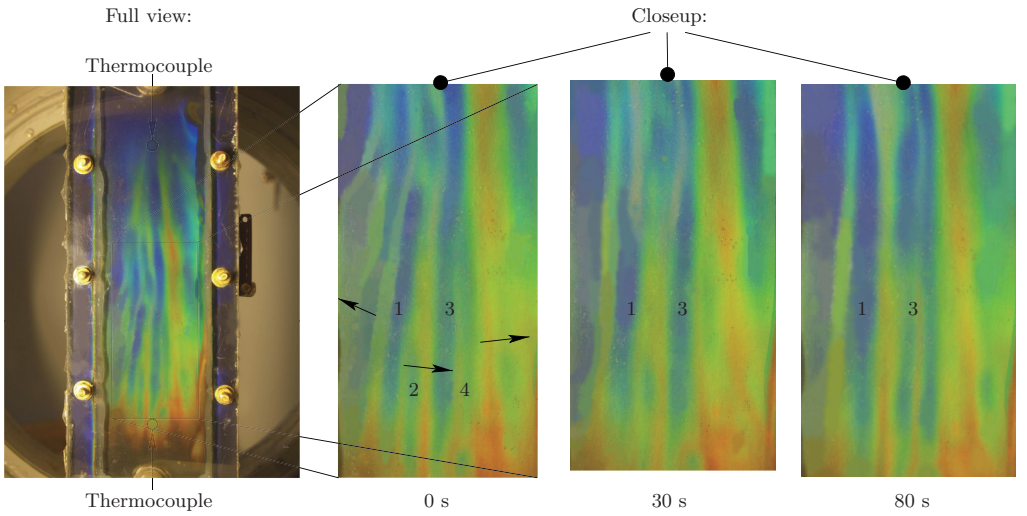

FIG. 11. (Color online) Temporal evolution of convection patterns at $\Delta T = 18.3$ K and $H = 21$ kA/m. Stationary rolls 1 and 3 are always present; traveling rolls 2 and 4 appear periodically. Arrows show the propagation directions of the local patterns. The width of the region depicted in the closeup images is 52 mm.

the layer. The time history of the output corresponding to the temperature difference τ between the brass heat exchanger and the location of the lower thermocouple is shown in Fig. 12 for an experimental run when the temperature difference between the chamber walls was maintained at $\Delta T = 18.3$ K and the applied magnetic field was increased in a stepwise manner from $H = 0$ to 7, 10, 14, 17, and, finally, 21 kA/m.

In the absence of the magnetic field the lower and upper thermocouples registered steady temperature differences of about 2.40 and 0.86 K, respectively. This difference in readings indicates the presence of a vertical temperature gradient of

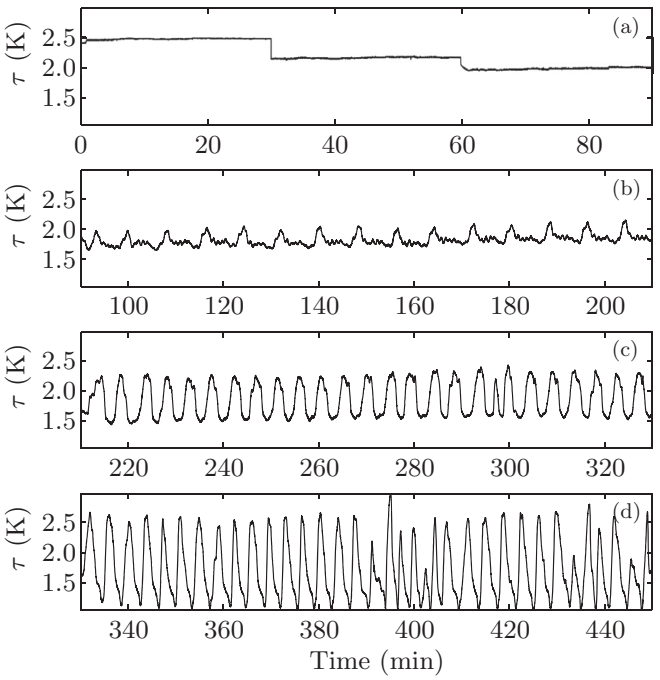

FIG. 12. Thermocouple readings for $\Delta T = 18.3$ K: (a) $H = 0$, 7, and 10.4 kA/m, (b) $H = 14$ kA/m, (c) $H = 17$ kA/m, and (d) $H = 21$ kA/m.

the order of $S = 10$ K/m in the vertical plane containing the thermocouples. Nondimensionally, this gives

$$\frac{SL}{\Delta T} \approx 0.14.$$

Because the thermocouples are located near the isothermal brass wall, this value is the lower bound estimation for the thermal stratification in the cavity. The universally accepted upper bound value of 0.5 was determined in the classical experiments reported in [63] for the center plane in the limit of large Gr. Therefore the corresponding value of the stratification parameter γ introduced in [57] and written in our notation is

$$3.3 < \gamma \equiv \left(8\frac{Sd}{\Delta T}\mathrm{GrPr}\right)^{1/4} < 4.5.$$

Then according to [57], Fig. 11] our experimental regimes ($\mathrm{Pr} \sim 1.3 \times 10^2$, $16\mathrm{Gr} \sim 1.1 \times 10^3$, where the factor of 16 is introduced to enable direct comparison with the cited figure) are very close to the $\mathrm{Gr}_c(\gamma)$ stability boundary of thermogravitational waves which increases steeply with stratification. This once again explains why no thermogravitational waves were detected in our experiments, and this is also consistent with their absence in numerical calculations of similar regimes reported in [64].

The thermocouple reading decreases abruptly when the magnetic field is switched on and then changes in a stepwise manner. The observed decrease in the temperature difference registered by thermocouples is attributed to the edge effects. Because of the difference in magnetic properties of the ferrocolloid and surrounding air, the applied uniform magnetic field is necessarily distorted near the edges of the chamber. The magnetic field gradient so induced, which depends on the strength of the applied field, leads to a toroidal fluid motion along the perimeter of the chamber. It manifests itself as narrow blue-green stripes on a liquid crystal film along the vertical edges of the chamber where the warm fluid from the back wall impinges on the sensor film. The intensity of these edge vortices increases with the field, leading to fluid mixing and,

subsequently, to the decrease of the temperature difference registered by the thermocouple as seen in Fig. 12(a).

The vertical thermomagnetic rolls were first detected visually at $H = 10.4$ kA/m. This convection pattern is stationary and it corresponds to the third horizontal line segment in Fig. 12(a). When the field was increased to $H = 14$ kA/m the thermocouple signal changed abruptly to a well-structured (ignoring noise) nonharmonic signal with a period of about 480 s. The corresponding Fourier spectrum shown in Fig. 13(a) indicates the presence of a fundamental harmonic with frequency $\nu_0 \approx 0.0021$ Hz as well as regularly spaced superharmonics with frequencies $2\nu_0$, $3\nu_0$, and $4\nu_0$. They arise due to a nonlinear self-interaction of the fundamental harmonic and do not represent physically distinct oscillatory modes. The spectrum also has a peak near zero frequency. It represents a slow variation of the average oscillation amplitude which is also a result of nonlinear self-interaction of the fundamental harmonic. Therefore we conclude that the first unsteady pattern arising when the field strength increased to 14 kA/m consists of a single nonlinear thermomagnetic wave. This is in agreement with the theoretical predictions of [20].

At $H = 17$ kA/m the period of the thermocouple signal is reduced to approximately 290 s and its spectrum undergoes a qualitative change; see Fig. 13(b). Instead of the regularly spaced well-defined superharmonics a relatively wide range of frequencies centered at $\nu_0 \approx 0.0035$ Hz appears. The widening of the spectrum near the main frequency and the disappearance of superharmonics observed here are similar to the perturbed flow behavior reported in [65]. It was shown there that increasing the degree of the supercriticality has a double effect on the perturbation characteristics. On one hand it widens the spectrum of unstable disturbances near the fundamental frequency (wave number); on the other it leads to a sideband instability that destroys harmonics whose frequencies are far apart from the main one. As a result the thermocouple signal shape becomes more sinusoidal, as seen in Fig. 12(c).

Increasing the magnetic field to $H = 21$ kA/m leads to yet another qualitative change: the periodic thermocouple response becomes modulated as seen in Fig. 12(d). This is the signature of a second oscillatory mode (thermomagnetic wave) with a nearby frequency appearing in the flow. The Fourier power spectrum shown in Fig. 13(c) has two satellite peaks corresponding to $\nu_1 \approx 0.0041$ Hz and $\nu_2 \approx 0.0047$ Hz near the base frequency of $\nu_0 = (\nu_1 + \nu_2)/2 \approx 0.0044$ Hz corresponding to the main period of 225 s. The modulation frequency $\nu_m = (\nu_2 - \nu_1)/2 \approx 0.0003$ corresponds to a modulation period which is about 15 times longer than the main oscillation period.

It is important to note that even though in the experimental run documented in Fig. 13 the magnetic field was maintained fixed for not more than 2 h for each field value, the period, the amplitude, and the shape of the oscillatory thermocouple signal remained unchanged in much longer (8–10 h) fixed-field runs for each of the tested field intensities. Therefore it is safe to state that the data obtained during the reported 2 h runs faithfully represent statistically steady regimes. Specifically, the thermocouple signal quantitatively confirms the existence of four main flow patterns predicted theoretically and detected visually in experiments: undisturbed up-down flow and its superposition with stationary vertical rolls, propagating waves,

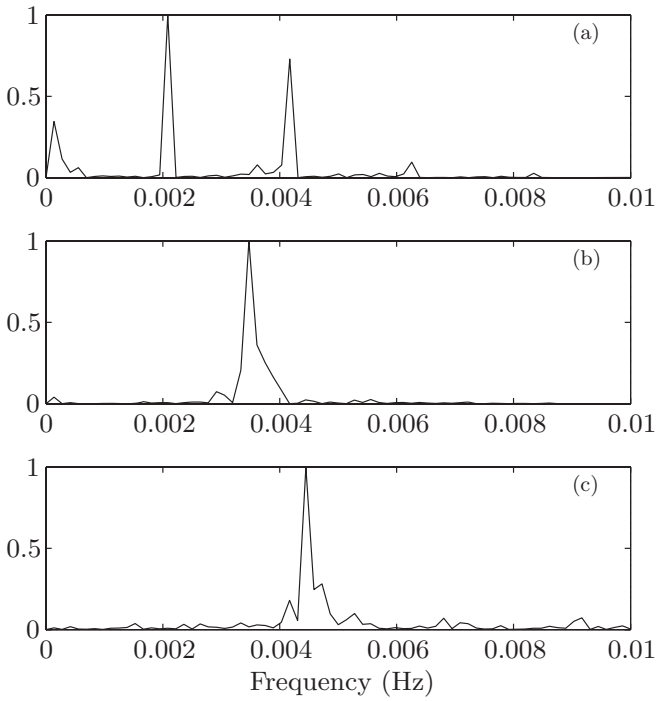

FIG. 13. Normalized Fourier spectrum of the thermocouple signal for $\Delta T = 18.3$ K: (a) $H = 14$ kA/m, (b) $H = 17$ kA/m, and (c) $H = 21$ kA/m.

and combinations of propagating waves. Although the detected frequencies of oscillations are somewhat smaller than those found computationally [see Fig. 2(c)], their qualitative behavior is in full agreement with the theoretical predictions: the thermomagnetic wave frequency increases with the magnetic field, i.e., with Gr_m [see the dashed line in Fig. 2(c)], and the second close frequency appears when the magnetic field becomes sufficiently strong [see the intersection of the dashed and solid lines in Fig. 2(c)].

V. CONCLUSIONS

Our analysis of the perturbation energy distribution across a vertical layer of a ferrofluid shows that the instability is caused by two physical mechanisms: thermogravitational (gravitational buoyancy) and thermomagnetic (magnetic buoyancy). These mechanisms result in four major types of perturbation flow patterns: counterpropagating thermogravitational waves (large Gr, small Gr_m), two types of counterpropagating thermomagnetic waves (large Gr_m, intermediate Gr), and stationary magnetoconvection rolls (intermediate to large Gr_m, small Gr). The transition between thermogravitational and thermomagnetic waves occurs when Gr and Gr_m are of comparable sizes. It is continuous in its nature so that conventional indicators such as a jump in a disturbance wave number or propagation speed cannot be used to detect it. Thus the quantitative criterion for determining the dominant mechanism at a given set of governing parameters is introduced based on disturbance energy considerations.

The spatial orientation of the detected instability patterns is found to be related to the physical mechanisms causing

them: the propagating thermogravitational or thermomagnetic instability waves form moving horizontal or inclined convection rolls, respectively, while stationary magnetoconvection rolls remain vertical. Such rolls appear at relatively small values of Gr_m and continue to dominate the flow as Gr_m increases, forming a stationary background over which the thermomagnetic waves propagate.

The experimentally measured and numerically determined values of wave numbers and wave speeds (frequencies) corresponding to various flow patterns are found to be in reasonable agreement, and so are the critical values of the Rayleigh number for stationary vertical thermomagnetic rolls. However, estimation of accurate experimental values of the nondimensional parameters involving fluid viscosity for other observed patterns faces difficulties due to the presence of a vertical thermal stratification, magnetoviscous and particle thermodiffusion effects, as well as the formation of magnetic particle aggregates, all leading to variations in fluid viscosity that are unquantified to date. The presence of vertical sidewalls is also found to influence the experimental observations in the near-edge regions where the parallel basic flow and uniform field assumptions used to make the theoretical analysis tractable fail. The use of a wider experimental chamber in future experiments is hoped to reduce the influence of the edge effects on the flows in question.

Despite these difficulties the experimental investigation undertaken, which focused on the study of magnetoconvective patterns, confirmed the existence of all four patterns predicted in [20] and interpreted from a physical point of view in Sec. III. Experimental observations also strongly indicate that different individual flow patterns identified in the modal linear analysis of [20] can coexist and interact with each other. Further analysis of this interaction requires nonlinear consideration, which is the subject of our current studies.

It will also be of importance to determine whether the wavelike patterns reported here are unique to magnetoconvection or could be found in other convective systems. The obvious candidate for such an exploration is convection in an annulus with corotating walls as described in the Introduction. However, in addition to the requirement of a narrow gap between the rotating walls, the following conditions have to be satisfied: (1) the annulus has to be long and its top and bottom surfaces need to be flat and horizontal rather than sloping or curved to prevent the formation of thermal Rossby waves [66]; (2) the working fluid has to be characterized by a large Prandtl number (typical values for kerosene- or oil-based magnetic fluids range between 60 and 130); (3) the Coriolis force must be small in comparison with other forces acting in the system; (4) the gravitational and centrifugal buoyancy forces should be of comparable sizes. We note also that a recent theoretical study of isothermal Taylor-Couette flow of a ferrofluid in a finite gap between two differentially rotating cylinders [67] found that, in contrast to our observations, a transverse magnetic field pins the developing instabilities, making them stationary. Therefore it appears that the competition between the thermal and magnetic mechanisms that we reported here is very important in defining flow patterns in ferrohydrodynamic systems of various configurations and thus it deserves further research effort.

ACKNOWLEDGMENTS

The numerical part of this work was completed using resources made available to S.A.S. by the Victorian Partnership for Advanced Computing. S.A.S. is grateful to Professor Will Phillips for supportive discussions.

[1] D. I. Ageikin, Proc. Acad. Sci. USSR **74**, 229 (1950) (in Russian).
[2] J. R. Carruthers and R. Wolfe, J. Appl. Phys. **39**, 5718 (1968).
[3] D. Braithwaite, E. Beaugnon, and R. Tournier, Nature (London) **354**, 134 (1991).
[4] T. Bednarz, J. C. Patterson, C. Lei, and H. Ozoe, Int. Commun. Heat Mass Transfer **36**, 781 (2009).
[5] V. G. Bashtovoy, B. M. Berkovsky, and A. N. Vislovich, *Introduction to Thermomechanics of Magnetic Fluids* (Hemisphere, Washington, DC, 1988).
[6] S. Odenbach, *Ferrofluids: Magnetically Controllable Fluids and Their Applications* (Springer, New York, 2002) .
[7] T. Kuwahara and H. Yamaguchi, J. Thermophys. Heat Transfer **21**, 173 (2007).
[8] T. Kuwahara, F. De Vuyst, and H. Yamaguchi, Phys. Fluids **21**, 097101 (2009).
[9] J. C. Boulware, H. Ban, S. Jensen, and S. Wassom, Exp. Therm. Fluid Sci. **34**, 1182 (2010).
[10] Q. Li, W. Lian, H. Sun, and Y. Xuan, Int. J. Heat Mass Transfer **51**, 5033 (2008).
[11] W. Lian, Y. Xuan, and Q. Li, Int. J. Heat Mass Transfer **52**, 5451 (2009).
[12] E. Ya. Blums, M. M. Maiorov, and A. O. Tsebers, *Magnetic Fluids* (Zinatne, Riga, Latvia, 1989) (in Russian).
[13] S. Odenbach, J. Magn. Magn. Mater. **149**, 155 (1995).
[14] A. Mukhopadhyay, R. Ganguly, S. Sen, and I. K. Puri, Int. J. Heat Mass Transfer **48**, 3485 (2005).
[15] A. A. Bozhko and G. F. Putin, Microgravity Sci. Technol. **21**, 89 (2007).
[16] The ponderomotive force appearing in nonconducting magnetic fluids is of Kelvin type and must be distinguished from the Lorentz-type driving force arising in magnetohydrodynamics of conducting fluids. The former is "static" in its nature as it depends only on the magnetization of the medium and can occur in systems with resting fluid, while the latter requires fluid motion.
[17] D. Zablotsky, A. Mezulis, and E. Blums, Int. J. Heat Mass Transfer **52**, 5302 (2009).
[18] C. M. Chang, W. T. Cheng, W. J. Liu, H. W. Cheng, C. E. Huang, and S. W. Du, Int. Commun. Heat Mass Transfer **37**, 801 (2010).
[19] J. Singh and R. Bajaj, Phys. Fluids **21**, 064105 (2009).
[20] S. A. Suslov, Phys. Fluids **20**, 084101 (2008).
[21] G. Z. Gershuni and E. M. Zhukhovitsky, Lett. Acad. Sci. USSR **4**, 12 (1981) (in Russian).

[22] A. N. Sharifulin, Lett. Acad. Sci. USSR **2**, 186 (1983) (in Russian).
[23] K. Gotoh and M. Yamada, J. Phys. Soc. Jpn. **51**, 3042 (1982).
[24] F. H. Busse, M. A. Zaks, and O. Brausch, Physica D **184**, 3 (2003).
[25] M. Jaletzky and F. H. Busse, Proc. Natl. Acad. Sci. USA **97**, 5060 (2000).
[26] A. A. Bozhko and G. F. Putin, Bull. Acad. Sci. USSR, Phys. Ser. **55**, 1149 (1991).
[27] A. A. Bozhko, T. V. Pilugina, G. F. Putin, D. V. Shupenik, and A. N. Suhanovsky in *Proceedings of the 8th International Conference on Magnetic Fluids*, edited by Yu. Ya. Schelykalov (Plyos, Russia, 1998), pp. 75–78.
[28] M. Kropp and F. H. Busse, Phys. Fluids A **3**, 2988 (1991).
[29] A. A. Bozhko and G. F. Putin, Magnetohydrodynamics **39**, 147 (2003).
[30] A. A. Bozhko, G. F. Putin, E. N. Beresneva, and P. V. Bulychev, Z. Phys. Chem. **220**, 251 (2006).
[31] S. A. Korpela, D. Gozum, and C. B. Baxi, Int. J. Heat Mass Transfer **16**, 1683 (1973).
[32] A. G. Kirdyashkin, A. I. Leont'ev, and N. V. Mukhina, Fluid Dyn. **6**, 884 (1971).
[33] G. Z. Gershuni, E. M. Zhukhovitsky, and A. A. Nepomniaschy, *Stability of Convective Flows* (Science, Moscow,1989) (in Russian).
[34] A. Chait and S. A. Korpela, J. Fluid Mech. **200**, 189 (1989).
[35] S. Wakitani, J. Fluid Mech. **314**, 299 (1996).
[36] D. A. Bratsun, A. V. Zyuzgin, and G. F. Putin, Int. J. Heat Fluid Flow **24**, 835 (2003).
[37] J. E. Hart, J. Fluid Mech. **47**, 547 (1971).
[38] L. S. Yao and B. B. Rogers, J. Fluid Mech. **201**, 279 (1989).
[39] S. A. Suslov and S. Paolucci, J. Fluid Mech. **302**, 91 (1995).
[40] S. Odenbach and K. Raj, Magnetohydrodynamics **36**, 312 (2000).
[41] S. Odenbach, *Magnetoviscous Effects in Ferrofluids* (Springer, New York, 2002).
[42] L. M. Pop and S. Odenbach, J. Phys.: Condens. Matter **18**, S2785 (2006).
[43] H. Engler, D. Borin, and S. Odenbach, J. Phys.: Conf. Ser. **149**, 012105 (2009).
[44] A. Lange, Phys. Rev. E **70**, 046308 (2004).
[45] A. Ryskin and H. Pleiner, Phys. Rev. E **69**, 046301 (2004).
[46] A. Ryskin and H. Pleiner, Phys. Rev. E **75**, 056303 (2007).
[47] T. Völker and S. Odenbach, Phys. Fluids **15**, 2198 (2003).
[48] A. V. Belyaev and B. L. Smorodin, J. Magn. Magn. Mater. **322**, 2596 (2010).
[49] The constitutive relationships suggested in the literature so far to account for the variation of ferrofluid viscosity with magnetic field still lack consistency and convincing experimental validation.
[50] B. A. Finlayson, J. Fluid Mech. **40**, 753 (1970).
[51] Note that Eq. (9) does not involve any approximations and is exact along the marginal stability boundary $\sigma^R = 0$. It should not be confused with fully nonlinear but approximate energy stability estimates discussed, for example, in [68].
[52] D. Hatziavramidis and H.-C. Ku, Comput. Math. Appl. **11**, 581 (1985).
[53] S. A. Suslov and S. Paolucci, J. Fluid Mech. **398**, 61 (1999).
[54] S. A. Suslov and S. Paolucci, J. Fluid Mech. **398**, 87 (1999).
[55] S. A. Suslov and S. Paolucci, Int. J. Heat Mass Transfer **38**, 2143 (1995).
[56] C. H. Vest and V. S. Arpachi, J. Fluid Mech. **36**, 1 (1969).
[57] R. F. Bergholz, J. Fluid Mech. **84**, 743 (1978).
[58] V. M. Buzmakov and A. F. Pshenichnikov, J. Colloid Interface Sci. **182**, 63 (1996).
[59] E. V. Lakhtina and A. F. Pshenichnikov, Colloid J. **68**, 327 (2006).
[60] P. Ilg, M. Kröger, and S. Hess, Phys. Rev. E **71**, 031205 (2005).
[61] P. Ilg, M. Kröger, and S. Hess, Phys. Rev. E **71**, 051201 (2005).
[62] See Supplemental Material at http://link.aps.org/supplemental/10.1103/PhysRevE.86.016301 for the video recording of the experiment.
[63] J. W. Elder, J. Fluid Mech. **23**, 77 (1965).
[64] Y. Lee and S. A. Korpela, J. Fluid Mech. **126**, 91 (1983).
[65] S. A. Suslov and S. Paolucci, Fluid Dyn. Res. **35**, 159 (2004).
[66] F. H. Busse and A. C. Or, J. Fluid Mech. **166**, 173 (1986).
[67] S. Altmeyer, Ch. Hoffmann, A. Leschhorn, and M. Lücke, Phys. Rev. E **82**, 016321 (2010).
[68] J. Singh, Phys. Rev. E **82**, 026311 (2010).